Transport Modelling of Flare Electrons

Jimmy Fitzpatrick

July 12, 2022

1 Background

Solar flares produce a multitude of electromagnetic (EM) emission [Fletcher et al. (2011)], and release vast amounts of energy [Shibata & Magara (2011)]. A portion of this energy is directed into particle accelerations, of particular attention is the acceleration of non-thermal electrons out of the background thermal plasma. These high energy electrons (> 40keV) can travel both downward, where they can collide with layers deeper in the solar atmosphere creating the HXR emission [Holman et al. (2011)], and outward into interplanetary space where they can be detected by instruments [e.g. WIND/3DP; Lin et al. (1995)]. These outwardly propagating beams can excite Langmuir waves in the ambient plasma, generating type III radio bursts which can also be observed [White et al. (2011)]. These observations of type III radio are often coincident with the arrival of the electrons and HXR emission, which is indicitave that these EM emissions may be created from the same electron population.

In the previous analysis, a transport model with instantaneous injection was used to fit omni-directional electron fluxes detected in-situ at 1AU by the WIND/3DP instrument. However, we can see that an improved modelling and analysis can be made by incorporating non-instantaneous injections [e.g. Wang et al. (2006); Agueda et al. (2009); Dröge et al. (2018)].

In the simplest model of electron release from the acceleration site in the flare event, and higher energy electrons (> 40keV) travel nearly scatter free towards to earth. In this case, the temporal and spectral shape of the electrons detected in-situ at 1AU should near exactly match the inferred solar electron spectrum determined through HXR observations. However, it was found that for some events, there was delayed arrival of the electrons with respect to injections inferred from electromagnetic emission [e.g. Dresing et al. (2021)]. Further, it is found that for some solar events the peak-flux spectrum of electrons observed at 1AU show inconsistencies with those inferred from HXR emission. For example, Krucker et al. (2007) show that for some prompt events (where the derived injection time coincides with HXR production) the HXR photon power-law spectral index, and the observed electron spectral index measured for higher energy electrons (> 50keV) show a good correlation. However, they are inconsistent with thin and thick target models of HXR production. It is also demonstrated that for some delayed events (derived injection time > 10 minutes after HXR production) there exists only a weak correlation. To note, these discrepancies are not as prevalent in smaller electron events such as those analysed by James et al. (2017). In any case, to explain the inconsistencies we investigate the importance of transport effects by incorporating pitch-angle scattering of the electron as they propagate through the IPM. Indeed, models with pitch-angle scattering have been shown to be very successful at reproducing particle flux observations at Earth [e.g. (Dröge et al., 2014); Dröge et al. (2018) ; Beeck & Wibberenz (1986); Agueda et al. (2009)]

By initialising simulations with injection functions deduced from observed HXR data, we can look into whether these observed electrons are of the same population producing this

HXR emission for a number of flare events. We will perform a detailed modelling of the angular-distributions of particles at 1AU, as well as omni-directional fluxes similar to figures produced within Dröge et al. (2018). By including a mean free path dependence on energy, we will perform a fitting to observed data [e.g. Alcock (2018)]. We will also investigate asymmetric magnetic field turbulence as described in section **??**.

2 Charged Particle Transport Along Turbulent Magnetic Fields

2.1 Transport Model

Electrons are accelerated to high energies by an arbitrary mechanism, and released from the flare into an open magnetic field line. Due to the electrons low momenta, we make the reasonable assumption that the electrons are stuck to the field line. In this way, we model the transport along the field line in one dimension. We use methods derived by Gardiner in the text 'Handbook of Stochastic Methods', and used by MacKinnon & Craig (1991) and Dröge et al. (2014) to model the transported electrons using a modified one dimensional Fokker-Planck Transport equation [see Agueda et al. (2014) and Roelof (1969)],

$$\underbrace{\frac{\partial f}{\partial t} + \mu v \frac{\partial f}{\partial z}}_{A} + \underbrace{\frac{v(1-\mu^2)}{2L_z}\frac{\partial f}{\partial \mu}}_{B} - \underbrace{\frac{\partial}{\partial \mu}\left[D_{\mu\mu}\frac{\partial f}{\partial \mu}\right]}_{C} = \underbrace{q(t,z,v,\mu)}_{D} \tag{1}$$

where $f = f(v,z,\mu,t)$ is the particle phase space density function. t, v are time and the velocity of the particles while z and μ are the distance along the field line and the electrons pitch angle respectively. Equation 1 describes the injection and evolution of the particle phase space density, and neglects adiabatic deceleration and convection. See Ruffolo (1995) for a more fully described focused transport model.

Term A describes the convection of the particles along the field line; B is the adiabatic focusing term; C describes the pitch angle scattering of the electrons and D describes the injection function of electrons into the field line.

Adiabatic focusing arises due to diverging magnetic field, $B = B(z)$ and the conservation of the electrons magnetic moment, $\mu = 0.5mv_\perp^2/B$. As it travels along the field the magnetic field B decreases, and so $v_\perp$ must also decrease, leading to an increase in parallel velocity. Adiabatic focusing is characterised by the focusing length given by,

$$L(z) = B(z)\left(-\frac{\partial B}{\partial z}\right)^{-1} \tag{2}$$

In our model, we take $B(z) \propto z^{-2}$, which also defines explicitly $L(z)$ above through simple calculation.

The magnetic field of the Sun is turbulent, featuring fluctuations over many length scales. If the length scale of the fluctuations is of comparable order to the electrons gyroradius then resonances can occur, leading to energy transfer between the electrons and the field. An initially instantaneous beam of electrons injected radially along a field line will be diffused after many repeated interactions with this turbulent field. To describe this we employ the quasi-linear diffusion coefficient as derived by Jokipii (1966) and thereafter modified by Beeck & Wibberenz (1986),

$$D_{\mu\mu} = \frac{3v}{2\lambda_\parallel(4-q)(2-q)}(1-\mu^2)(|\mu|^{q-1}+h) \tag{3}$$

where we note that $\lambda_\parallel$ is the mean free path, q is the spectral index of the magnetic fluctuations. We use here a Kolmogorov spectrum of $q = 5/3$ in order to remain consistent

with previous literature. The term h is added to resolve that scattering is greatly reduced at μ near zero. We choose a small value of $h = 0.01$.

We modify Equation 3 by invoking a mean free path dependence on energy and distance along the field line according to,

$$\lambda_\parallel(z,p) = \lambda_{\parallel,\oplus} \left(\frac{z}{z_\oplus}\right)^\kappa \left(\frac{p}{p_0}\right)^{2\alpha} \tag{4}$$

where p is the particle momentum, p_0 is the momentum of the lowest energy particle considered (27 keV). $\lambda_{\parallel,\oplus}$ is the constant defined by the mean free path of the lowest energy particle considered at $z = z_\oplus$, where $z_\oplus$ is the position of the observing near Earth satellite. We fix $\kappa = 0.5$, as obtained by Alcock (2018), and make no assumptions on the value of α.

We find the velocities of the particles with the following relativistic equation, Kleppner (2014), given as

$$v(E) = c\sqrt{1 - \frac{m_e^2 c^4}{(E + m_e c^2)^2}} \tag{5}$$

with the energy, E, taken as the corresponding energy bins used by the WIND/3DP instrument.

2.2 Numerical Scheme

Analytical solutions to Equation 1 are not known and numerical schemes must be employed. We will use Monte Carlo simulations to model the evolving particle phase space distributions. In particular, using methods derived by Gardiner in the text 'Handbook of Stochastic Methods', and used by MacKinnon & Craig (1991) and Dröge et al. (2014), we transform Equation 1 into the equivalent stochastic differential equations,

$$z_{i+1} = z_i + \mu_i v \Delta t \tag{6}$$

$$\mu_{i+1} = \mu_i + \left(\frac{\partial D_{\mu\mu,i}}{\partial \mu} + \frac{v(1-\mu_i^2)}{2L_{z,i}}\right)\Delta t + \sqrt{2D_{\mu\mu,i}\Delta t}\,\xi \tag{7}$$

These sets of equations define the evolving position and pitch-angle of a single pseudo-particle injected into the system. The subscript i defines the timestep, while the random variable ξ is drawn from normally distributed pool of mean 0 and variance 1. By injecting a large number of pseudo-particles,and properties of the phase space density function are inferred through measuring the set of all the particles. To ensure numerical stability, we use timsteps defined by $\Delta t = \tau/100$ where the diffusive timescale is defined by $\tau = \lambda_\parallel/v$.

3 Analytical Verifications

In order to confirm the validity of the simulation, we perform comparisons with various analytical cases. By sampling our simulation accordingly, we can model observed electron fluxes at 1AU and compare these with expected fluxes in different scattering regimes and with different forms of injection function.

In this section, for simplicity we take the injection function $q(t,z,v,\mu) = q(z,t,\mu)$ as a step function defined by,

$$q(z,t) = \begin{cases} \delta(z - z_{\text{inj}})C & \text{if } t \in [t_1, t_2], \\ 0 & \text{else} \end{cases}$$

where the injection occurs over the time period t_1 to t_2, while the constant C is so defined to preserve total number of particles injected into the simulation, $N_\mathrm{p} = \int_0^\infty q(t)dt$. All particles are injected at a given $z = z_\mathrm{inj}$, with μ randomly sampled from an appropriate range (in the following, either radially beamed or isotropic). This model is favourable since we can also easily model instantaneous injections with t_1 approaching t_2, which also allows for comparisons in instantaneous cases.

3.1 Weak Scattering

In the weak scattering case we consider values of $\lambda_{\parallel,\oplus} \gg 1$. First, we employ an injection function of the form provided by Equation 3 with t_1 approaching t_2 modelling an instantaneous injection. All particles are beamed radially with μ near one and $z_\mathrm{inj} = 0.05$. We compare results of the model with the arrival times expected for ballistic particles experiencing no scattering. In particular, for the ballistic arrivals we plot the expected arrival time given by the simple distance-time calculation according to,

$$t_\mathrm{ETA} = \frac{z_\mathrm{obs} - z_\mathrm{inj}}{v(E)} \tag{8}$$

where z_obs is the location at which particles are sampled in the simulation, z_inj is the injection location and $v(E)$ is the respective velocity of the particles considered of energy E (related through Equation 5). We also plot the actual arrival time of a particle ran through the simulation with no scattering. Simulated electron fluxes are demonstrated in Figure 1, for weakly scattered particles with $\lambda_{\parallel,\oplus} = 50\mathrm{AU}$. Other relevant parameters are included in the figure. We find that indeed, the weakly scattered particles arrive near coincidentally with the expected ballistic arrival times, with all particles passing the modelled detector.

We also present another non-instantaneous case in the weak scattering limit, now with t_1 and t_2 distinct. As expected, we find that all particles arrive at the modelled detector, and the injection function is preserved during transport. This is demonstrated in in Figure 2 with the simulated electron flux mimicking the injection function shapewise, with temporal onset expected for weakly scattered particles and the observed duration equal to injection duration.

In summary, in the weak scattering limit we find behavior is as expected for the two forms of injection considered. Temporal onsets match those of a ballistic particle and duration of observed flux matches or is near injection duration. As expected, all particles pass the modelled detector. The good agreement continues with varying $\lambda_{\parallel,\oplus}$, α and over energy. Vector code working as expected.

3.2 Strong Scattering

A similar treatment is made now in the strong scattering limit with $\lambda_{\parallel,\oplus} \ll 1$. Following a similar derivation as by Kontar et al. (2013), it can be found that Equation 1 becomes,

$$\frac{\partial f}{\partial t} = D_{zz} \frac{\partial^2 f}{\partial z^2} + q(z,t) \tag{9}$$

where we have assumed that $q(t,z,v,\mu) = q(z,t)$, with also that $D_{zz} = v\lambda_\parallel/3$. A sketch derivation can be found in the appendix at the end of the document. Using Fourier methods, we can derive that the general solution is of the form,

$$f(z,t) = \int_{-\infty}^\infty f_0(s)G(z-s,t)ds + \int_0^t \int_{-\infty}^\infty G(z-s,t-\tau)q(s,\tau)dsd\tau \tag{10}$$

where $f_0(z)$ describes the initial phase space distribution and $G(z,t)$ is the heat kernel,

4

$$G(z,t) = \frac{1}{\sqrt{4\pi D_{zz}t}} \exp\left(-\frac{z^2}{4D_{zz}t}\right) \tag{11}$$

The integrations in Equation 10 can be explicitly carried out for both instantaneous and constant injection at $z = z_{\text{inj}}$. By injecting a population of electrons homogenous in μ (i.e. with μ randomly distributed between -1 and 1), and using a standard isotropic diffusion coefficient,

$$D_{\mu\mu} = \frac{v}{2\lambda_\parallel}(1 - \mu^2) \tag{12}$$

and neglecting the focusing term, we can compare our modelled flux at 1AU with that predicted by the analytical solutions in the two cases of injection function introduced above.

In the case of instantaneous injection at $z = z_{\text{inj}}$, we find that the particle phase-space distribution is,

$$f(z,t) \propto \frac{1}{\sqrt{4\pi D_{zz}t}} \exp\left(-\frac{\bar{z}^2}{4D_{zz}t}\right) = G(\bar{z}, t) \tag{13}$$

where $\bar{z} = z - z_{\text{inj}}$. Comparisons with simulated flux and analytical predictions can be found in Figure 3. We can see that for an instantaneous injection function, the modelled flux matches well that predicted by Equation 13.

In the case of non-instantaneous, constant injection at $z = z_{inj}$ we find that the particle phase-space distribution satisfies,
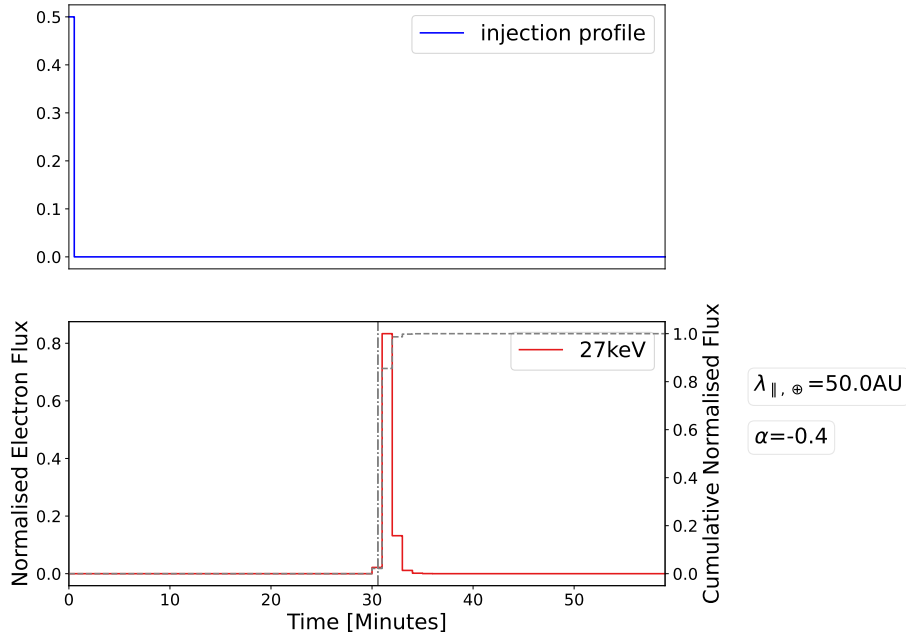

Figure 1: Lower panel displays the simulated electron flux at 1 AU (red curve) obtained from near-instantaneously injected 27 keV electrons from $t_1 = 0$ to $t_2 = t_{\text{end}}/100 \ll 1$, where t_{end} is the simulation run time. Grey dashed curve is the cumulative flux of incoming particles, while the vertical dashdotted curves indicate the expected arrival times of ballistic particles. In the top panel, is the injection function. All curves are normalised to the total number of particles. Simulation was run with $N_{\text{p}} = 50000$ pseudo-particles, $\lambda_{\parallel,\oplus} = 50$ AU and $\alpha = -0.4$ and sampled at $z = 1.2$ AU along the Parker spiral.
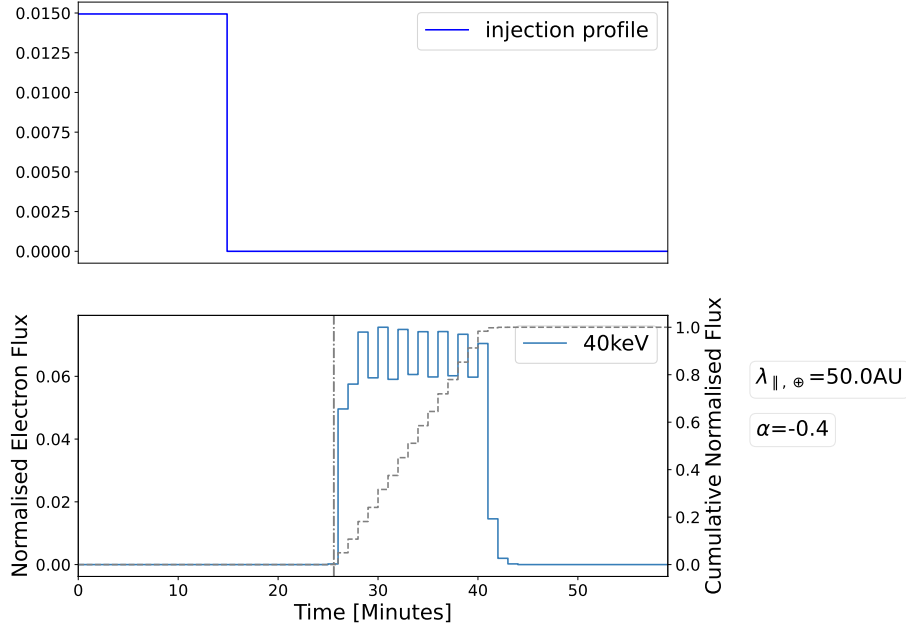
Figure 2: Lower panel displays the simulated electron flux at 1 AU (blue curve) obtained from injecting a constant stream of 40 keV electrons from $t_1 = 0$ to $t_2 = t_\mathrm{end}/4$, where t_end is the simulation runtime. Grey dashed curve, vertical dashdotted curves are as in Figure 1. As before, injection function is displayed in the top panel. All curves are normalised to the total number of particles. Simulation was run with $N_\mathrm{p} = 50000$ pseudo-particles, $\lambda_{\parallel,\oplus} = 50$ AU and $\alpha = -0.4$ and sampled at $z = 1.2$ AU along the parker spiral

$$f(z,t) \propto \sqrt{\frac{D_{zz}t}{\pi}} \exp\left(\frac{-\bar{z}^2}{4D_{zz}t}\right) + \frac{1}{2}\left[\bar{z}\,\mathrm{erf}\left(\frac{\bar{z}}{\sqrt{4D_{zz}t}}\right) - |\bar{z}|\right] \tag{14}$$

where $\mathrm{erf}(x)$ is the standard error function defined as,

$$\mathrm{erf}(x) = \frac{2}{\sqrt{\pi}}\int_0^x e^{-t^2}dt \tag{15}$$

Comparisons with simulated flux and analytical predictions can be found in Figure 4. Again, we find that the modelled flux matches well with that predicted by Equation 14.

In summary, we have shown that there is good agreement between the simulated flux and analytical predictions in both cases of the injection function presented above. The good agreement continued with varying $\lambda_{\parallel,\oplus}$ and over energy. Vector code working as expected.

To note, in the above, a modified flux measuring method was implemented as opposed to that that will be used in the fitting and in the weak scattering section. Since particles are likely to be scattered backwards and forwards, previous method of 'counting once' led to underestimates of particle counts with higher t. In the strong scattering cases, the code counts particles with positions, z, that satisfy $z_\mathrm{obs} - \mathrm{tol} \times z_\mathrm{obs} < z < z_\mathrm{obs} + \mathrm{tol} \times z_\mathrm{obs}$. In the above, we took $\mathrm{tol} = 0.1$ but found good agreement with variations in this value.

The asymmetric model agrees well with the symmetric model in the case that $\lambda_{\parallel,\oplus}^+ = \lambda_{\parallel,\oplus}^-$, for a wide range of inputted pairs of mean free paths. The simulation step size is defined using the minimum mean free path of all the pairs of mean free paths. To be shown.
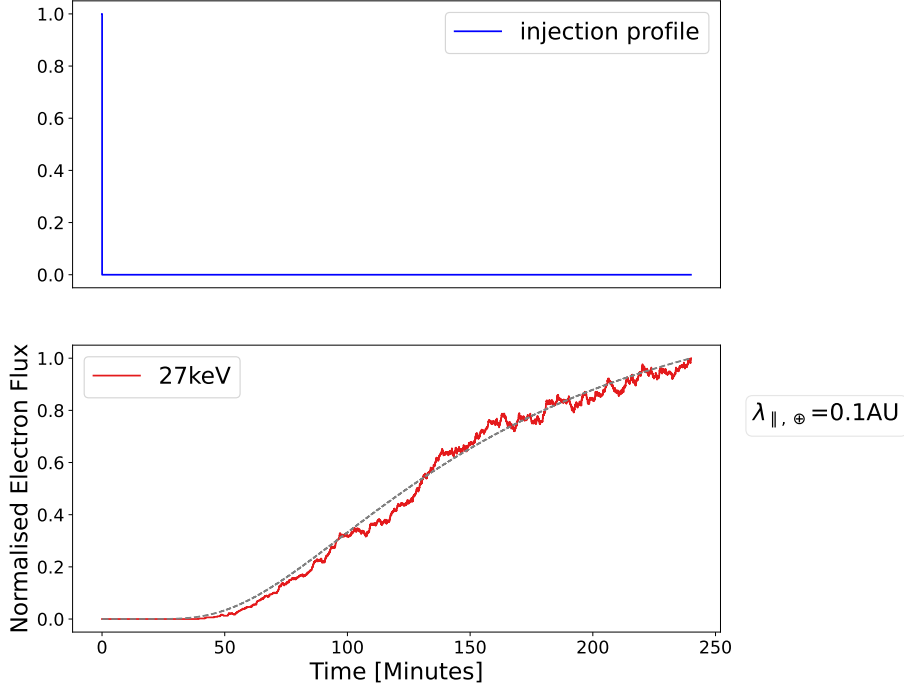
6

Figure 3: Lower panel compares the simulated electron flux (red curve) at 1AU, with that predicted by Equation 13 (grey dashed). Simulated flux and analytical prediction are normalised to their respective maxima. The top panel reveals the injection function normalised to the total number of particles injected; the 27 keV electrons are instantaneously injected at the first time-step (specifically, $t_1 = 0$ and $t_2 = t_{\text{end}}/10000$). Simulation was run with $N_{\text{p}} = 10000$ pseudo-particles, $\lambda_{\parallel,\oplus} = 0.1$ AU, $\alpha = 0.0$ and sampled at $z = 1.2$ AU along the parker spiral

4   Asymmetric Turbulence

4.1   A Simplified Model of Asymmetric Turbulence

A simplified model of asymmetric turbulence is implemented by splitting the constant $\lambda_{\parallel,\oplus}$ as defined above into two components depending on the particles pitch angle,

$$\lambda_{\parallel,\oplus} = \begin{cases} \lambda_{\parallel,\oplus}^+ & \text{if } \mu > 0, \\ \lambda_{\parallel,\oplus}^- & \text{if } \mu < 0, \end{cases}$$

with the corresponding diffusion coefficients and related variables (i.e. equations 3 and 4), now piece-wise defined for $\mu > 0$ and $\mu < 0$ so that,

$$D_{\mu\mu}^{(\text{asym})} = \begin{cases} D_{\mu\mu}|_{\lambda_{\parallel,\oplus}^+} & \text{if } \mu > 0, \\ D_{\mu\mu}|_{\lambda_{\parallel,\oplus}^-} & \text{if } \mu < 0, \end{cases}$$

This is implemented into the model outlined in the previous sections, with findings presented below.

We consider pairs of mean free paths $[\lambda_{\parallel,\oplus}^-, \lambda_{\parallel,\oplus}^+]$, with pairs sampled from $[0.5, 1.0, 10.0]$. The model is verified against the previous (symmetric) model, by considering pairs so that $\lambda_{\parallel,\oplus}^- = \lambda_{\parallel,\oplus}^+$. Results are also compared to the symmetric model with $\lambda_{\parallel,\oplus} = \lambda_{\parallel,\oplus}^+$ for all $\mu \in [-1, 1]$. The ratio $R = D_{\mu\mu}^+/D_{\mu\mu}^-$ is a measure of the relative strengths of scattering in the forwards ($\mu > 0$) and backwards ($\mu < 0$) directions.
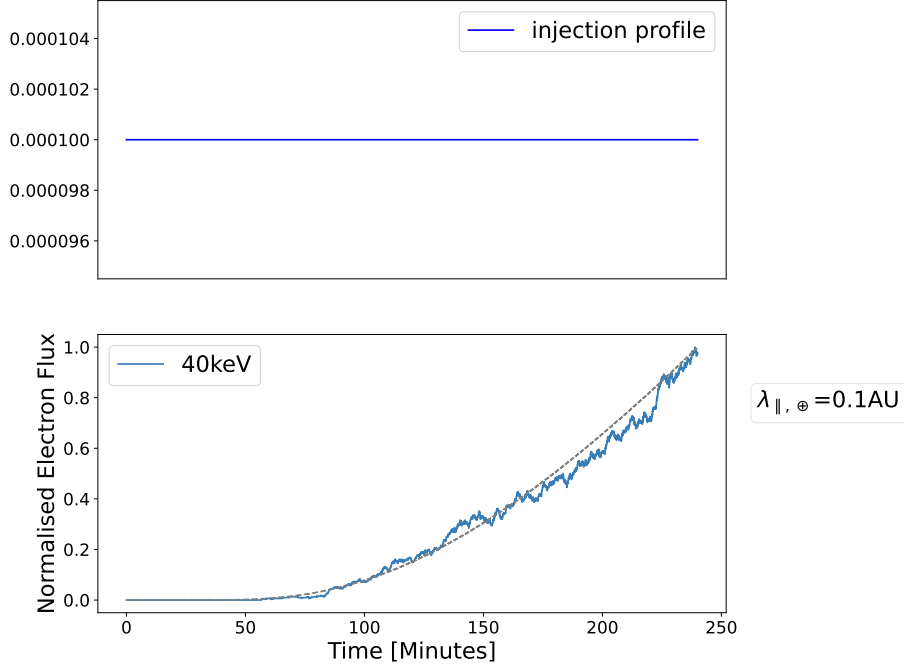
Figure 4: Lower panel compares the simulated electron flux (blue curve) at 1AU, with that predicted by Equation 14 (grey dashed). Simulated flux and analytical prediction are normalised to their respective maxima. The top panel reveals the injection function normalised to the total number of particles injected; the 40 keV electrons constantly injected throughout the simulation (setting $t_1 = 0$ to $t_2 = t_{\text{end}}$). Simulation was run with $N_{\text{p}} = 10000$ pseudo-particles, $\lambda_{\parallel,\oplus} = 0.1$ AU, $\alpha = 0.0$ and sampled at $z = 1.2$ along the parker spiral

Not shown (though available in google drive) is the agreement between the symmetric model and asymmetric model for a variety of mean free paths. Figure 5 and 6 show a comparison of the asymmetric model with a symmetric model as described above. It is noted that there is little difference between the simulated fluxes in the limiting case of weak scattering in the forward direction, R=0.1. This is expected behaviour since the μ distribution should stay near 1 (tbc with μ distribution sampling). Though, in the case of R=10 (strong scattering in the forward direction) there is a decided difference between the simulated fluxes. To determine whether this is reasonable behaviour further investigation is required.

4.2 Validations with the Symmetric Case

Due to discrepancies between analytical cases derived for the asymmetric case, we consider verifications in the symmetric case of strong diffusion. We consider a similar treatment as in Section 3.2. In the following, we compare the symmetric model (computed with $\lambda_{\parallel,\oplus} = \lambda_{\parallel}$ constant), the asymmetric model (with $\lambda_{\parallel}^+ = \lambda_{\parallel}^- = \lambda_{\parallel}$ constant) with the analytical solutions in the case of constant and instantaneous injection in the strong diffusion limit. Importantly, no adjustments have been made to the simulation timestep!

Figures 7 and 8 present the results of the analysis. We find good agreement between the symmmetric, asymmetric simulations and analytical solutions in these cases. Increasing agreement is present with decreasing $\lambda_{\parallel}$. All simulations are run with 5000 injected test particles at $z_{\text{inj}} = 0.05$ AU.

Figure 7 shows simulation are run with $\lambda_{\parallel} = 0.01$, with an instantaneous injection of 27 keV electrons. Good agreement between the symmetric, asymmetric models and analytic solution (Equation 13) is found. Not displayed, but available in the google drive is the agree-
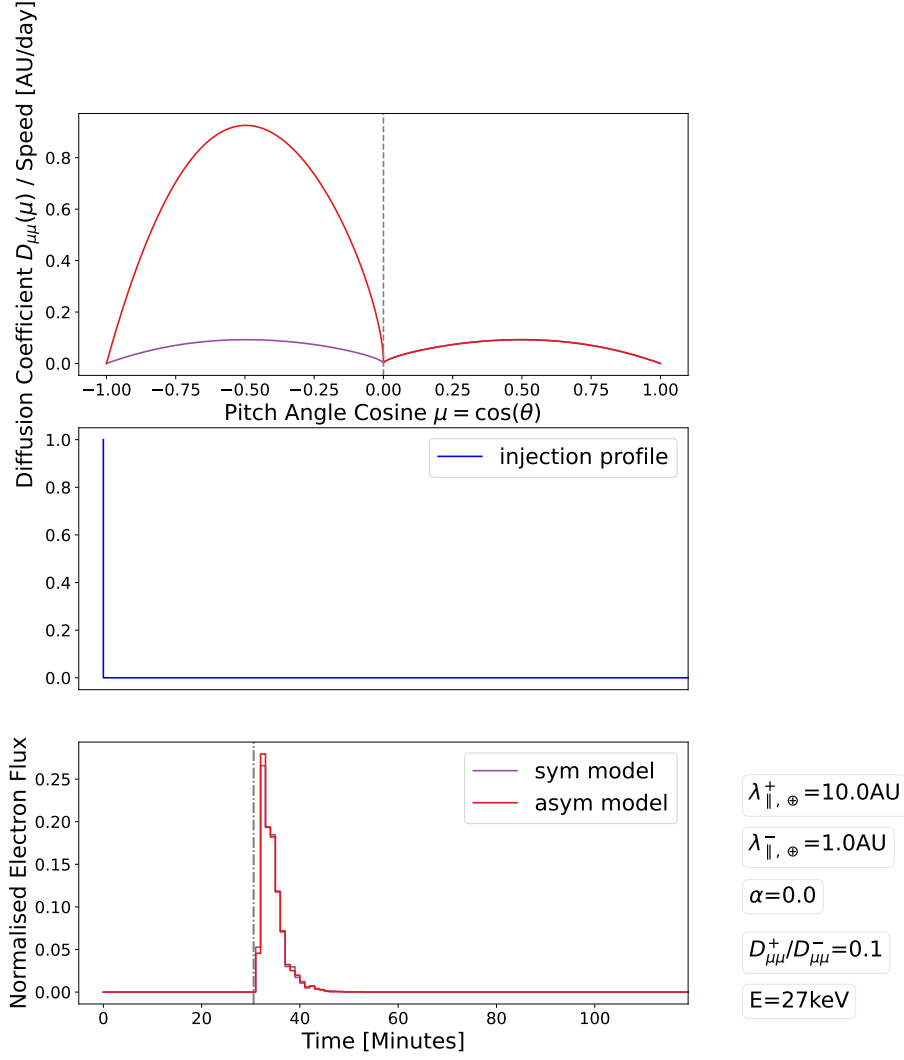
Figure 5: A comparison of the simulated fluxes for the asymmetric model and symmetric model in the case of weak scattering in the forward direction. Top panel presents the normalised diffusion coefficients for the two models. Middle panel displays the (instantaneous) injection function, with electrons injected at $z_{\mathrm{inj}} = 0.05$ AU. Bottom panel shows the respective fluxes sampled at $z = 1.2$ AU. The different mean free path; relative strengths of scattering and other parameters are shown in the figure. Expected arrival times are shown in the dashed lines. Simulation is ran with 10000 test particles.

ment for $\lambda_{\parallel} = 0.1$ AU. Particles are intialised with an isotropic mu distribution.

Figure 8 shows simulation are run with $\lambda_{\parallel} = 0.01$, with a constant injection of 27 keV electrons throughout the simulation run time. Good agreement between the symmetric, asymmetric models and analytic solution (Equation 14) is found. Not displayed, but available in the google drive is the agreement for $\lambda_{\parallel} = 0.1$ AU. For 0.1 AU, the number of injected particles was increased to 15 000 to minimise statistical errors.
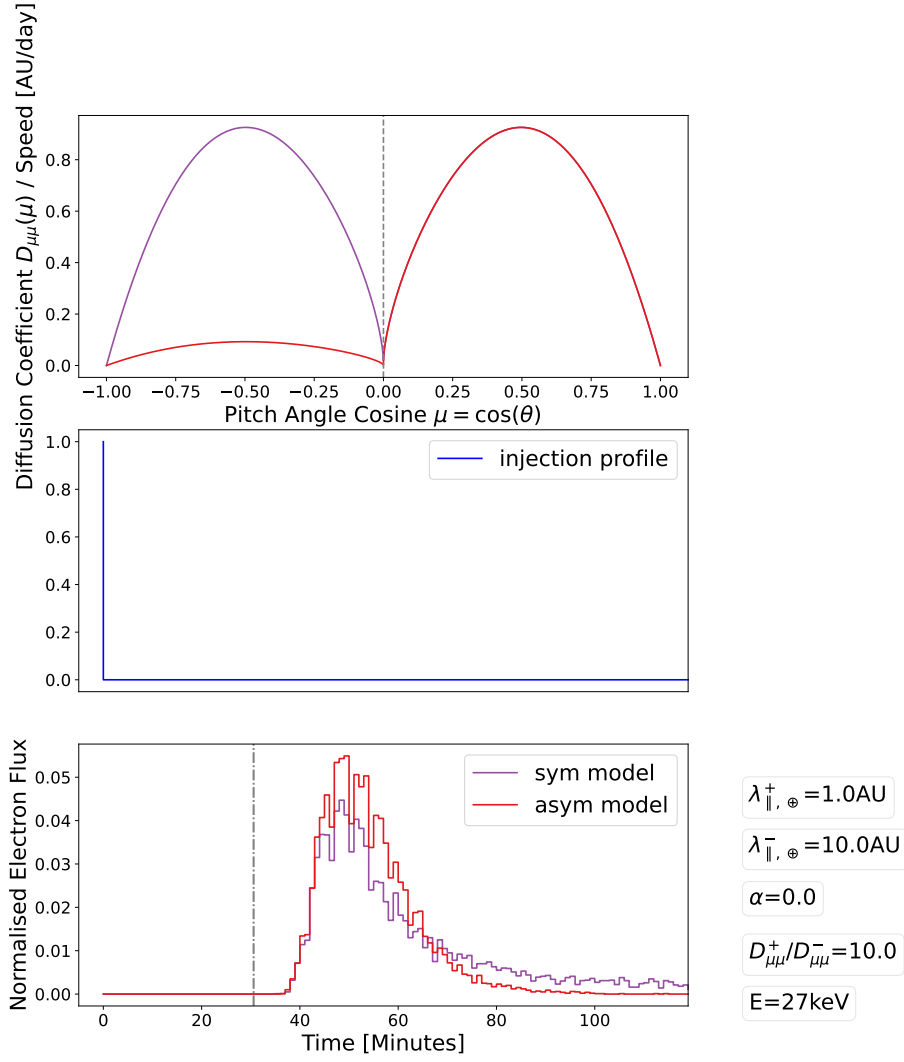
9

Figure 6: Identical to Figure 5 but in the case of strong scattering in the forward direction. The different mean free path; relative strengths of scattering and other parameters are shown in the figure. Note, the decided difference between the two fluxes.

References

Agueda, N., Klein, K. L., Vilmer, N., et al. 2014, A&A, 570, A5

Agueda, N., Lario, D., Vainio, R., et al. 2009, A&A, 507, 981

Alcock, B. 2018, Solar electron and radio propagation in the turbulent solar corona, PhD thesis, University of Glasgow, Podunk IN

Beeck, J. & Wibberenz, G. 1986, ApJ, 311, 437

Dresing, N., Warmuth, A., Effenberger, F., et al. 2021, A&A, 654, A92

Dröge, W., Kartavykh, Y. Y., Dresing, N., Heber, B., & Klassen, A. 2014, Journal of Geophysical Research (Space Physics), 119, 6074

Dröge, W., Kartavykh, Y. Y., Wang, L., Telloni, D., & Bruno, R. 2018, ApJ, 869, 168

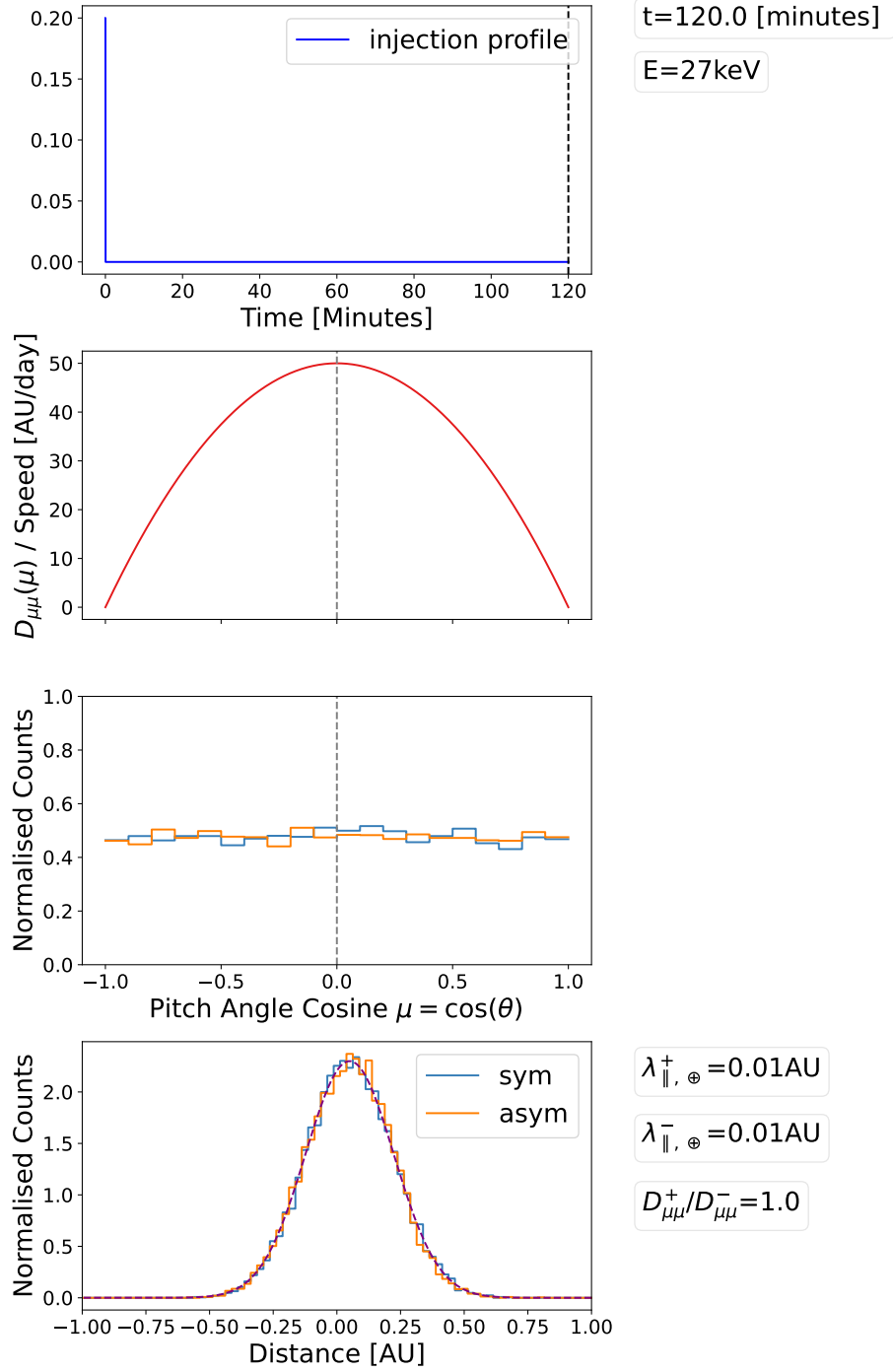Fletcher, L., Dennis, B. R., Hudson, H. S., et al. 2011, Space Sci. Rev., 159, 19

Figure 7: Figure shows the good agreement between the symmetric and asymmetric models with the analytical solution (Equation 13) in the case of instantaneous injection. Top panel shows the injection function (blue), with horizontal dashed line showing the time of sampling. Second panel diplays the isotropic form of $D_{\mu\mu}$ with which the simulation was evaluated. Third panel displays the mu distribution of the symmetric and asymmetric models. Bottom panel shows the z distribution of both models (solid) overlayed with the analytical solution. Simulation was run with $\lambda_\parallel = 0.01$ AU, and injected with 5000 particles. z,mu distributions and the analytical solution are area normalised, injection function is normalised to the total number of injected particles.
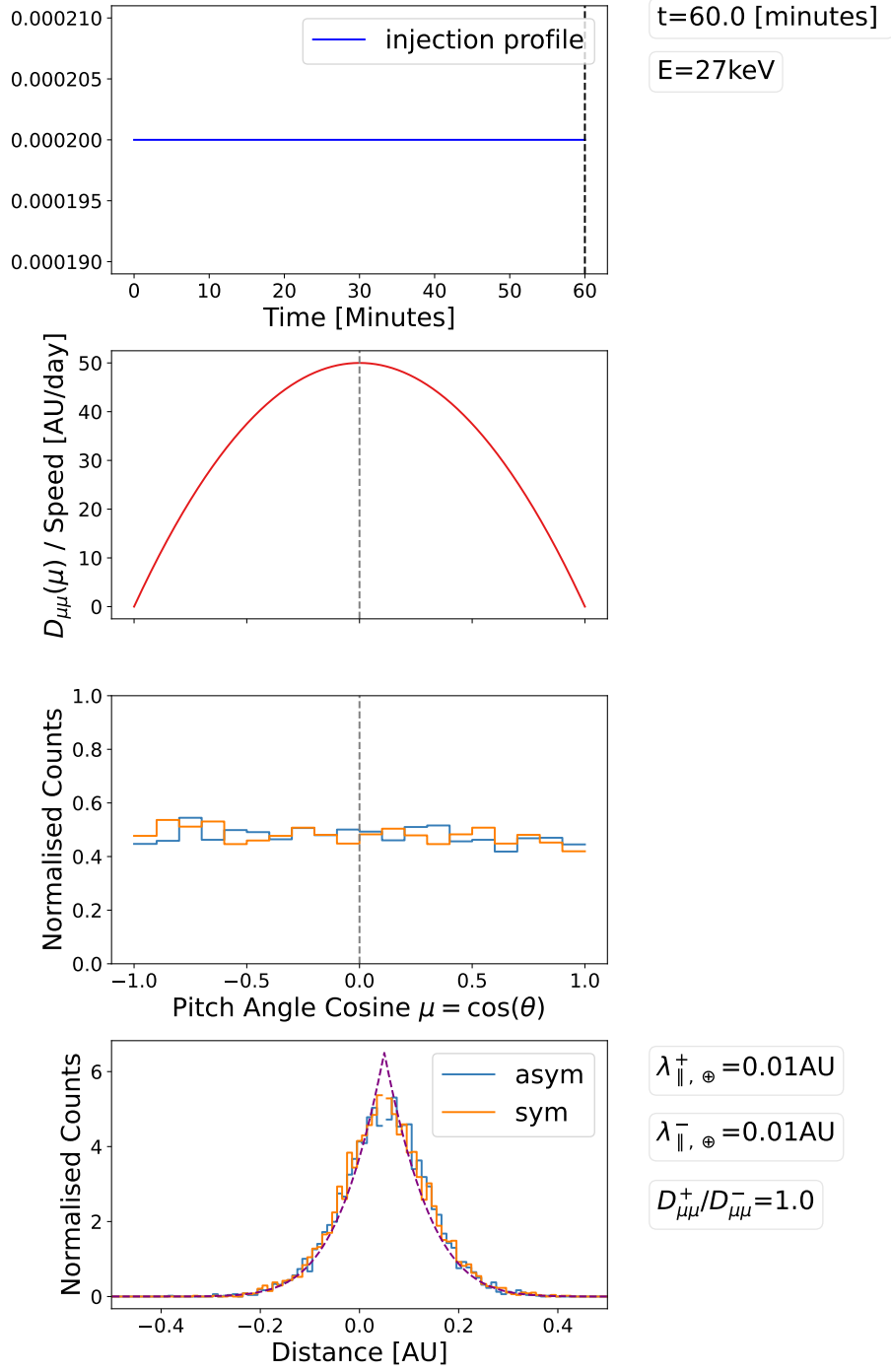
Figure 8: Identical as Figure 7 but in the case of constant injection throughout the simulation run time. In this case, the analytical solution is provided by Equation 14. The bin that contains the injection location has been removed to not skew the simulated distributions (all particles are held here until release).

Holman, G. D., Aschwanden, M. J., Aurass, H., et al. 2011, Space Sci. Rev., 159, 107

James, T., Subramanian, P., & Kontar, E. P. 2017, Monthly Notices of the Royal Astronomical Society, 471, 471

Jokipii, J. R. 1966, ApJ, 146, 480

Kleppner, D. 2014, An introduction to mechanics / Daniel Kleppner, Robert Kolenkow., second edition. edn. (Cambridge: Cambridge University Press), 489

Kontar, E. P., Bian, N. H., Emslie, A. G., & Vilmer, N. 2013, The Astrophysical Journal, 780, 780

Krucker, S., Kontar, E. P., Christe, S., & Lin, R. P. 2007, ApJ, 663, L109

Lin, R. P., Anderson, K. A., Ashford, S., et al. 1995, Space Sci. Rev., 71, 125

MacKinnon, A. L. & Craig, I. J. D. 1991, A&A, 251, 693

Roelof, E. C. 1969, in Lectures in High-Energy Astrophysics, ed. H. Ögelman & J. R. Wayland, 111

Ruffolo, D. 1995, ApJ, 442, 861

Schlickeiser, R. 1989, ApJ, 336, 243

Shibata, K. & Magara, T. 2011, Living Reviews in Solar Physics, 8, 8

Wang, L., Lin, R. P., Krucker, S., & Gosling, J. T. 2006, Geophys. Res. Lett., 33, L03106

White, S. M., Benz, A. O., Christe, S., et al. 2011, Space Sci. Rev., 159, 225

Appendix

Sketch Derivation of Strong Scattering PDE

Note that the pitch-angle diffusion coefficient can be written,

$$D_{\mu\mu} = D_{\mu\mu}^{(T)} + D_{\mu\mu}^{(C)} \tag{16}$$

thus consisting of a collisional and turbulent term. For strong pitch-angle scattering $D_{\mu\mu}^{(T)} \gg 1$, leading to a flattening of the particle phase-space distribution in μ in time. In other words, $\partial f/\partial \mu \to 0$. Further, in this limit the operator describing convection along the field line becomes (on average) a spatial diffusion parallel to the guiding field,

$$\mu v \frac{\partial f}{\partial z} \to D_{zz} \frac{\partial^2 f}{\partial z^2} \tag{17}$$

where we have introduced the spatial diffusion coefficient D_{zz}, which involves an average of the pitch-angle diffusion over pitch angles, according to:

$$D_{zz} = \frac{v^2}{8} \int_{-1}^{1} \frac{(1-\mu^2)^2}{D_{\mu\mu}^{(T)}} d\mu = \frac{v\lambda_{\parallel}}{3} \tag{18}$$

where $\lambda_{\parallel}$ is the mean free path of the electrons. Important note, to write the above we have assumed that $\lambda_{\parallel}$ is constant. Explicitly, [e.g. in Schlickeiser (1989)] $\lambda_{\parallel}$ is described through,

$$\lambda_{\parallel} = \frac{3v}{8} \int_{-1}^{1} \frac{(1-\mu^2)^2}{D_{\mu\mu}^{(T)}} \tag{19}$$

One can see that using the relationship 17 and that $\partial f/\partial \mu \to 0$ then Equation 1 becomes,

$$\frac{\partial f}{\partial t} = D_{zz} \frac{\partial^2 f}{\partial z^2} + q(z,t) \tag{20}$$